

Article

Piezotronic and Piezo-Phototronic Effects-Enhanced Core–Shell Structure-Based Nanowire Field-Effect Transistors

Xiang Liu ^{1,2}, Fangpei Li ^{1,2,3,*}, Wenbo Peng ^{1,2,*} , Quanzhe Zhu ⁴, Yangshan Li ⁴, Guodong Zheng ⁴, Hongyang Tian ⁴ and Yongning He ^{1,2,*}

¹ School of Microelectronics, Xi'an Jiaotong University, Xi'an 710049, China

² The Key Lab of Micro-Nano Electronics and System Integration of Xi'an City, Xi'an 710049, China

³ State Key Laboratory of Solidification Processing, Key Laboratory of Radiation Detection Materials and Devices, School of Materials Science and Engineering, Northwestern Polytechnical University, Xi'an 710072, China

⁴ Shaanxi Advanced Semiconductor Technology Center Co., Ltd., Xi'an 710077, China

* Correspondence: fangpeilee@163.com (F.L.); wpeng33@mail.xjtu.edu.cn (W.P.); yongning@mail.xjtu.edu.cn (Y.H.)

Abstract: Piezotronic and piezo-phototronic effects have been extensively applied to modulate the performance of advanced electronics and optoelectronics. In this study, to systematically investigate the piezotronic and piezo-phototronic effects in field-effect transistors (FETs), a core–shell structure-based Si/ZnO nanowire heterojunction FET (HJFET) model was established using the finite element method. We performed a sweep analysis of several parameters of the model. The results show that the channel current increases with the channel radial thickness and channel doping concentration, while it decreases with the channel length, gate doping concentration, and gate voltage. Under a tensile strain of 0.39‰, the saturation current change rate can reach 38%. Finally, another core–shell structure-based ZnO/Si nanowire HJFET model with the same parameters was established. The simulation results show that at a compressive strain of −0.39‰, the saturation current change rate is about 18%, which is smaller than that of the Si/ZnO case. Piezoelectric potential and photogenerated electromotive force jointly regulate the carrier distribution in the channel, change the width of the channel depletion layer and the channel conductivity, and thus regulate the channel current. The research results provide a certain degree of reference for the subsequent experimental design of Zn-based HJFETs and are applicable to other kinds of FETs.

Keywords: piezotronic; piezo-phototronic; core–shell structure; ZnO; heterojunction field-effect transistor



Citation: Liu, X.; Li, F.; Peng, W.; Zhu, Q.; Li, Y.; Zheng, G.; Tian, H.; He, Y. Piezotronic and Piezo-Phototronic Effects-Enhanced Core–Shell Structure-Based Nanowire Field-Effect Transistors. *Micromachines* **2023**, *14*, 1335. <https://doi.org/10.3390/mi14071335>

Academic Editors: Antonio Di Bartolomeo, Arun Kumar and Valeria Demontis

Received: 9 June 2023
Revised: 28 June 2023
Accepted: 28 June 2023
Published: 29 June 2023



Copyright: © 2023 by the authors. Licensee MDPI, Basel, Switzerland. This article is an open access article distributed under the terms and conditions of the Creative Commons Attribution (CC BY) license (<https://creativecommons.org/licenses/by/4.0/>).

1. Introduction

As a third-generation electronic material, wide bandgap semiconductor materials have the advantages of high carrier mobility, strong radiation resistance, and high breakdown field strength. They have been applied in various fields such as photodetectors [1–4], surface acoustic wave devices [5,6], and solar cells [7–9]. Zinc oxide (ZnO) semiconductor material not only has excellent light absorption performance in the ultraviolet (UV) band due to its wide bandgap of 3.37 eV but also possesses excellent piezoelectric properties originating from its non-centrosymmetric crystal structure. Prof. Zhong Lin Wang invented the piezotronic effect in 2006, which is defined as the mechanical stimulus-induced piezoelectric polarization charges modulation on the performances of electronic devices [10]. After its invention, the piezotronic effect developed rapidly in different kinds of advanced electronic devices, with a focus on the Schottky or PN junction.

By further introducing optical excitation to the piezotronic effect, the piezoelectric and optoelectronic effects can jointly regulate the photo-excited carrier transport in semiconductors, which was invented by Prof. Zhong Lin Wang in 2010 and named the piezo-phototronic effect [11–15]. Using multi-effect coupling for semiconductor materials to design new electronic devices is an effective means of optimizing device performance

and improving the integration of on-chip devices. By utilizing the piezotronic and piezophototronic effects, various high-performance electronic and optoelectronic devices can be realized [16–21]. For example, Yiyao Peng et al. prepared a self-powered flexible UV photodetector based on p-GaN/n-ZnO heterostructure, the relative optical response of which can be increased to 22% after applying -0.48% compressive strain under UV irradiation of 38.4 mW/cm^2 [21].

Compared with a bipolar junction transistor, the channel resistance of a field-effect transistor (FET) has a negative temperature coefficient and better thermal stability. Among them, due to the lack of insulation layer capacitance, the junction FET (JFET) requires low gate driving power, a simple preparation process, and can achieve smaller device size. At present, there have been many studies on ZnO-based FETs [22–27], but most of them are the metal-oxide-semiconductor FETs (MOSFETs) or metal-semiconductor FETs (MESFETs), and there is less theoretical and experimental research on ZnO-based JFETs [28,29]. In 2019, Nan Guo et al. prepared a light-driven WSe_2 -ZnO JFET with n-ZnO nanosheets as the gate material, and the device's optical response reached $4.83 \times 10^3 \text{ A/W}$, with a response time of $10 \mu\text{s}$ [29]. In addition, the tunneling field-effect transistor (TFET) as another promising candidate has been extensively studied due to its capability of lowering the subthreshold swing down to even less than 60 mV/decade [30]. Several studies in the literature have built the core-shell nanowire heterojunction structure-based TFET model and studied its characteristics, presenting superior performances compared to conventional MOSFET [31–33]. Moreover, bipolar junction transistors also own huge potentials in high-performance optoelectronic devices and the piezo-phototronic effect could be further utilized to optimize its characteristics [34].

Recently, our group developed a Si/ZnO thin-film-based heterojunction FET (HJFET) model (p-Si as channel) and theoretically studied its performances as modulated by the piezotronic and piezo-phototronic effects [35]. The analytical equations of Si/ZnO thin-film-based HJFET have been derived theoretically. However, during the theoretical derivation, necessary assumptions must be applied to the model so that analytical equations could be obtained. In addition, the carrier distribution inside the whole HJFET under different strain/light/electric conditions could not be mapped directly, which is not beneficial for understanding and analyzing the beneath working mechanisms.

As the size of transistors continues to decrease, in order to maintain the control of channel current by the gate, field-effect transistors have developed from traditional single gate to multi-gate to the gate-all-around structure. In this work, we establish a core-shell structure-based Si/ZnO nanowire HJFET model utilizing the finite element method. The piezotronic and piezo-phototronic effects on its performances have been systematically simulated and analyzed. The carrier distribution could be obtained and utilized to understand the working mechanism. This work helps to improve the theory of piezotronic and piezo-phototronic effects in JFETs and could be expanded to other kinds of FETs.

2. Simulation Model and Finite Element Method

Partial differential equations are often used to describe the state of the carriers inside a device. However, for most problems, they are difficult to solve analytically. By discretizing the partial differential equations, approximate numerical model equations are obtained, and the solutions of these numerical model equations are approximate solutions to the corresponding real solutions. The finite element method (FEM) is used to calculate these approximate solutions. All research in this paper is based on the finite element analysis software COMSOL Multiphysics.

As mentioned above, regarding the theoretical derivation of piezotronic and piezophototronic effects in ZnO-based HJFET, our research group has previously achieved some results [35]. Based on the previous model, here we established a core-shell structure-based Si/ZnO nanowire HJFET model using the finite element method to further verify the theoretical derivation of piezotronic and piezo-phototronic effects in ZnO-based HJFET. For the established simulation model, the p-Si core nanowire is used as the p-channel, and the

n-ZnO shell is used as the gate, which is a p-channel HJFET. The n-channel HJFET has also been investigated by using the n-ZnO core nanowire as the n-channel and the p-Si shell as the gate. The parameters of Si and ZnO used in the simulation are shown in Table 1.

Table 1. Parameters for Si and ZnO semiconductors.

Material Parameters	Si	ZnO
Relative dielectric constant	11.7	(8.5446, 8.5446, 10.204)
Electron lifetime (μs)	10	10
Hole lifetime (μs)	10	10
Band gap (eV)	1.12	3.37
Electron affinity (eV)	4.05	4.5
Valence band effective density of states (cm^{-3})	1.04×10^{19}	3.5×10^{18}
Conduction band effective density of states (cm^{-3})	2.8×10^{19}	1×10^{20}
Electron mobility ($\text{cm}^2 \cdot \text{V}^{-1} \cdot \text{s}^{-1}$)	1450	200
Hole mobility ($\text{cm}^2 \cdot \text{V}^{-1} \cdot \text{s}^{-1}$)	500	10

In classical piezoelectric theory, piezoelectric charges are often treated as surface charges because the distribution region of polarization charges is far smaller than the size of piezoelectric block materials. In our established HJFET model, we introduce the externally applied strain through the surface charge density boundary condition. The piezoelectric equation includes:

$$(\mathbf{P})_i = (e)_{ijk}(\varepsilon)_{jk} \quad (1)$$

In the formula, \mathbf{P} is the polarization vector/ $\text{C} \cdot \text{m}^{-2}$; $(e)_{ijk}$ is the third-order piezoelectric tensor; ε is the strain tensor. According to the C_{6v} symmetry of ZnO crystal (wurtzite structure), when only the c -axis direction of ZnO is externally applied with strain ε_3 , the corresponding polarization vector \mathbf{P} can be obtained from Equation (1):

$$P_1 = P_2 = 0, P_3 = e_{33}\varepsilon_3 \quad (2)$$

For ZnO piezoelectric semiconductor, e_{33} is usually taken as $1.22 \text{ C} \cdot \text{m}^{-2}$. Assuming that the width of piezoelectric polarization charge distribution on the ZnO surface is w_{piezo} , then the piezoelectric charge density N_{piezo} is:

$$N_{piezo} = \frac{P_3}{qw_{piezo}} \quad (3)$$

At the same time, we introduce incident light illumination through a customized carrier generation boundary condition, and the generation rate of photo-excited charge carriers is related to incident light wavelength, light intensity, and material absorption coefficient. At the same time, the Shockley–Read–Hall (SRH) recombination model is added to the model, which uses the constant minority carrier lifetime shown in Table 1.

3. Results and Discussion

3.1. Basic Characteristics and Piezotronic and Piezo-Phototronic Effects on p-Channel Core–Shell Structure-Based HJFET

Firstly, the simulation model of a p-channel core–shell structure-based HJFET is illustrated in the inset of Figure 1a. It could be seen that the radius of p-channel Si is a and the radius of whole device is $a + b$. The channel length is defined as L . Unless otherwise specified, the simulation parameters of the p-channel HJFET model are shown in Table 2.

The basic output characteristics of the device are shown in Figure 1. Figure 1a shows the transfer characteristics, and Figure 1b shows the output characteristics. It can be seen from the simulation results that the device indeed exhibits distinctive p-channel HJFET characteristics. At $V_{GS} = 0 \text{ V}$, the channel is not fully depleted by n-ZnO gate and therefore current could flow in the p-channel with V_{DS} applied. With the increase in V_{GS} , obviously

the channel becomes fully depleted and the flowing current in the p-channel decreases. At $V_{GS} = 0.3$ V, the device almost turns off and the gate control effect is obvious. If we select the on-state voltage as ($V_{GS} = 0$ V, $V_{DS} = -5$ V) and the off-state voltage as ($V_{GS} = 1$ V, $V_{DS} = 0$ V), the switching ratio of the device reaches as high as 2.665×10^{10} . The output characteristic curves under different gate voltages are also consistent with expectations. When $V_{GS} = 0$ V and $V_{DS} = -5$ V, the channel current I_D is about $-0.557 \mu\text{A}$. As the gate voltage increases, the channel current decreases, making it easier to reach saturation at the same drain-source voltage.

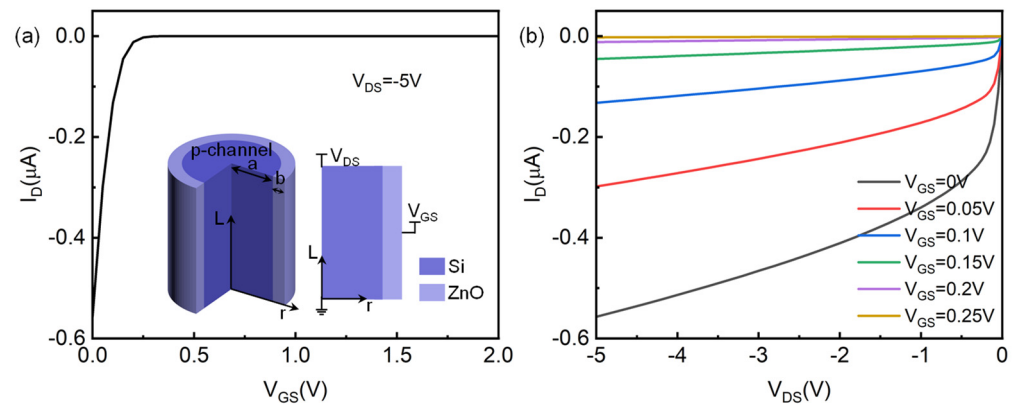


Figure 1. Simulation model and basic characteristics of p-channel HJFET. (a) Transfer characteristics. The inset shows the established model and its cross-sectional view. (b) Output characteristics.

Table 2. Parameters for p-channel HJFET model.

Parameters	Value
Radius of core Si nanowire (a)	0.35 μm
Thickness of shell ZnO (b)	0.1 μm
Channel length (L)	1 μm
Acceptor doping concentration in Si (N_A)	$1 \times 10^{16} \text{ cm}^{-3}$
Donor doping concentration in ZnO (N_D)	$1 \times 10^{18} \text{ cm}^{-3}$

For the introduction of strain in p-channel HJFET, by assuming that strain induced piezoelectric charges are distributed near the core–shell Si/ZnO heterojunction interface in the area with a width w_{piezo} of 1 nm, the corresponding piezoelectric charge density N_{piezo} can be obtained by Equation (3). According to the theoretical calculation in the previous section, when the strain ϵ_3 is 0.3‰, the strain-induced piezoelectric charge density is about $1 \times 10^{18} \text{ cm}^{-3}$ scale. Figure 2 shows the changes in the electrical properties of p-channel HJFET after introducing strain. From Figure 2a, it can be seen that after applying tensile strain ($\epsilon_3 > 0$), the channel current I_D increases, and after applying compressive strain ($\epsilon_3 < 0$), the channel current I_D decreases. The strain varies within the range of -0.39% to 0.39% , achieving a monotonic saturation current I_{Dsat} increase of $-0.4 \mu\text{A} \sim -0.77 \mu\text{A}$. The corresponding saturated drain-source voltage V_{Dsat} also increases. As shown in Figure 2b, the corresponding saturation current change rate can reach 38%, where the current change rate $\Delta I/I_0$ is defined as $(I_{Dsat-\epsilon} - I_{Dsat-\epsilon=0})/I_{Dsat-\epsilon=0}$. Figure 2c shows the changes in the saturation current of the device when a larger strain range is applied. The direction of strain regulation remains unchanged, that is, after applying tensile strain, the channel current I_D increases. More importantly, when the tensile strain is increased to around 1%, the I_D reaches saturation with increasing tensile strain, which is about $-110 \mu\text{A}$. After applying compressive strain, the channel current change is opposite, with the I_D even decreasing nearly to zero. This indicates that the strain regulation itself owns a broad modulation capability of the channel current I_D .

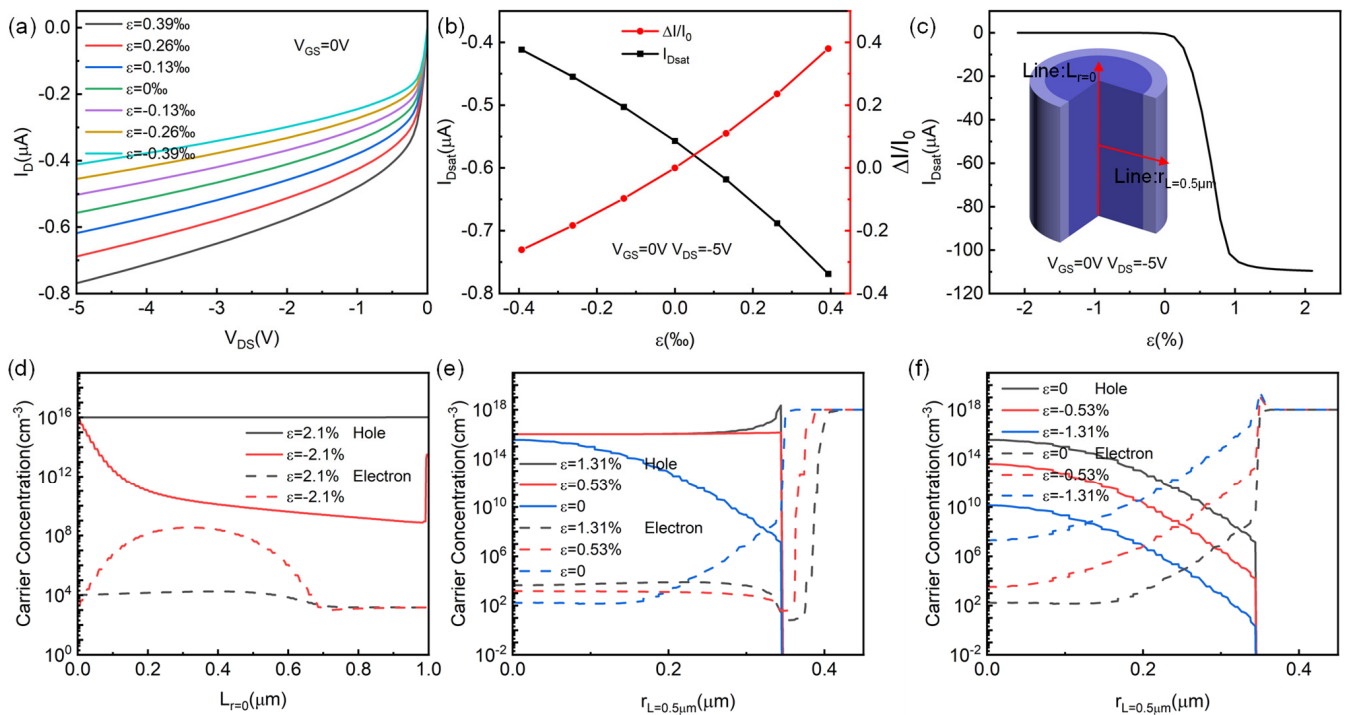


Figure 2. Applying strain on p-channel HJFET. (a) Output characteristics of HJFET after strain application. (b) Saturated current I_{Dsat} and its rate of change $\Delta I/I_0$ with applied strain. (c) Change of saturation current I_{Dsat} after increasing the range of applied strain. The internal illustration is the schematic diagram of the selected position. (d) Carrier concentration distribution at the device’s central axis under different strain conditions. (e) Carrier concentration distribution at the device’s central horizontal line under tensile strain. (f) Carrier concentration distribution at the device’s central horizontal line under compressive strain.

Figure 2d–f show the carrier concentration distribution at different positions (Line: $L_{r=0}$ and Line: $r_{L=0}$) of the device after the strain is applied. The schematic diagram of the selected line position is shown in the inset illustration in Figure 2c. The dashed lines in Figure 2d–f represent the electron concentration distribution, and the solid lines represent the hole concentration distribution. From Figure 2d, it can be seen that, when a large tensile strain of 2.1% is applied, the hole concentration in the channel reaches about the order of $1 \times 10^{16} \text{ cm}^{-3}$, which is close to the acceptor doping concentration in the p-Si channel. This indicates that the bias voltage of $V_{GS} = 0 \text{ V}$ and $V_{DS} = -5 \text{ V}$ cannot saturate the channel current of the device. Therefore, the saturated channel current in Figure 2c under larger tensile strain conditions will actually be higher. After applying a large compressive strain of -2.1% , the hole concentration as p-channel carriers decreases dramatically and, hence, the channel has been turned off by the externally applied compressive strain. Figure 2e,f show the carrier concentration distribution of the device’s central horizontal line under tensile and compressive strains, respectively. It can be seen from Figure 2e that after the tensile strain is applied, the width of the depletion region on the p-Si channel side decreases, while the width of the depletion region on the n-ZnO gate side increases. As a result, the p-channel carrier concentration increases, leading to an increase in the channel current I_D . After the compression strain is applied, the change in depletion region of both sides is opposite, just as shown in Figure 2f.

In order to analyze the regulatory effect of strain on the electrical performance of p-channel HJFET more clearly, Figure 3 provides a detailed schematic diagram of the p-channel HJFET. The c -axis direction of ZnO layer is always radial. Figure 3a shows the HJFET without external bias, and Figure 3b shows the HJFET controlled by bias voltage. For a p-channel HJFET, when the gate voltage V_{GS} is positive, the gate PN junction is reverse

biased, the width of the depletion region increases, the conduction area of the p-channel decreases, the channel resistance increases, and, finally, the channel current decreases. At the same time, when the negative drain-source voltage V_{DS} is applied, the gate junction reverse bias voltage at the drain end is greater, thus the width of the depletion region further increases until the channel is completely depleted, that is, “channel pinch-off”. At this time, if the V_{DS} continues to increase, most of the voltage drops in the channel pinch-off area, and the channel current would no longer increase. Figure 3c,d show the strain regulated HJFET. After the tensile strain is applied, negative piezoelectric polarization charges are induced at the Si/ZnO heterostructure interface, attracting holes and repelling electrons, resulting in a decrease in the p-channel depletion region, an increase in the p-channel conduction area, and thus an increase in the channel current I_D . The opposite modulation would be produced when the compressive strain is applied, as illustrated by Figure 3d. Figure 3e–h provides the cross-sectional views of the logarithmic distribution of charge carriers under tensile and compressive strains, which together with Figure 2e,f validate the above strain regulation working mechanism analysis.

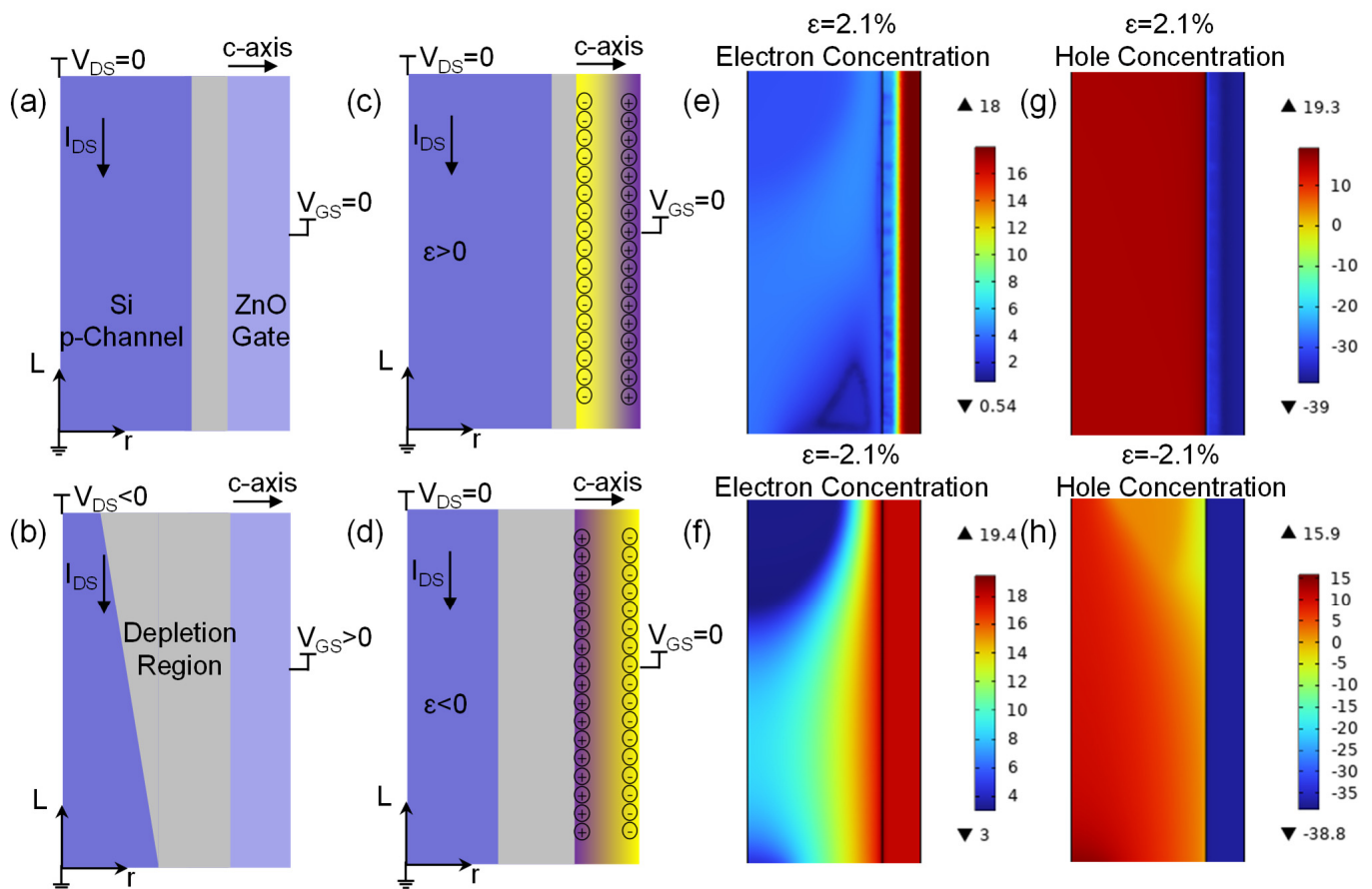


Figure 3. Schematic diagram of the analysis of strain regulation effect on p-channel HJFET. (a,b) Schematic diagram of p-channel HJFET under bias voltage regulation. (c,d) Schematic diagram of p-channel HJFET under tensile and compressive strain regulation. (e–h) Logarithmic distribution of carrier concentrations obtained from simulation under both bias voltage and strain regulation.

In our established simulation model, we also introduced incident light illumination through a customized generation boundary condition to study the performance changes in the device under different light conditions, namely, only the p-Si channel layer and only the gate n-ZnO layer have photo-generated carriers. Figure 4 shows the optical response performance of the p-channel HJFET. Figure 4a,d present the corresponding output characteristic changes when the generation rate is adopted only in the p-Si channel and the n-ZnO gate, respectively. It can be seen that at the same level of photo-generated carrier generation rate,

the photo-generated carriers in p-Si have a greater impact on the electrical performance of the device compared to that in n-ZnO. From Figure 4c, it can be seen that when the photo-generated carrier generation rate of Si ($G_{ph_{Si}}$) is $1 \times 10^{24} \text{ cm}^{-3} \cdot \text{s}^{-1}$, the minority carrier (electron) concentration in the p-channel increases to the order of $1 \times 10^{12} \text{ cm}^{-3}$, and the channel current I_D varies from $-0.557 \mu\text{A}$ in the dark state to $-0.606 \mu\text{A}$. The saturation current change rate reaches about 9%, where the current change rate $\Delta I/I_0$ is defined as $(I_{D_{\text{sat-Gph}}} - I_{D_{\text{sat-Gph}=0}})/I_{D_{\text{sat-Gph}=0}}$. From Figure 4f, when $G_{ph_{ZnO}}$ is $1 \times 10^{24} \text{ cm}^{-3} \cdot \text{s}^{-1}$, although the minority carrier (hole) concentration on the ZnO side reaches $1 \times 10^{14} \text{ cm}^{-3}$, since most of the depletion region is located in the p-Si channel, the photo-generated electromotive force is small and has little effect on device's performance regulation. Therefore, the saturation current change rate is less than 3%. Our simulation results show that under the same carrier generation rate, the regulation of photogenerated carriers in the channel is stronger. However, in the experimental design of Si/ZnO HJFET, light intensity and wavelength are the direct factors.

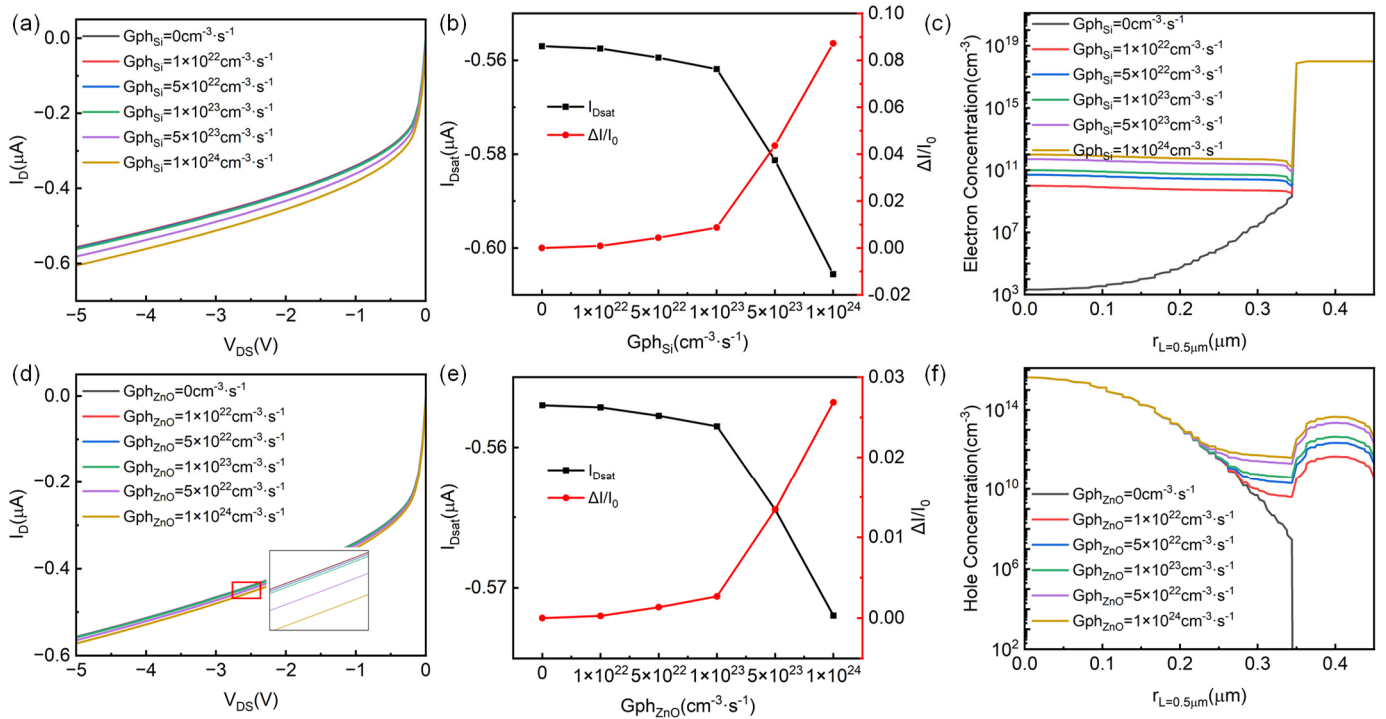


Figure 4. Applying light on p-channel HJFET. The output characteristics of p-channel HJFET with photo-generated carriers in (a) p-Si channel layer only and (d) gate n-ZnO layer only. (b,e) are the saturation current $I_{D_{\text{sat}}}$ and its rate of change $\Delta I/I_0$ respectively with the photo-generated carrier production rate $G_{ph_{Si}}$ in Si and $G_{ph_{ZnO}}$ in ZnO. (c,f) are the electron concentration distribution (as minority carrier in p-Si channel) and hole concentration distribution (as minority carrier in n-ZnO gate) at the central horizontal line position of the p-channel HJFET under different light conditions, respectively.

By introducing both strain and light into the p-channel HJFET, the simulation results show that the saturation channel current in HJFET varies with strain under different light conditions, as shown in Figure 5. From Figure 5a,c, it can be seen that when tensile strain is applied, the saturation channel current increases, while when compressive strain is applied, it is the opposite. Furthermore, after introducing light, the saturation channel current also increases, and the photo-generated carriers in p-Si channel have a greater regulatory effect on the device, consistent with the aforementioned phenomenon. When $G_{ph_{Si}} = 1 \times 10^{24} \text{ cm}^{-3} \cdot \text{s}^{-1}$, the saturated channel current is $-0.606 \mu\text{A}$, and the generated photocurrent is approximately $0.049 \mu\text{A}$. From Figure 5b,d, it can be seen that, compared

to the light regulation, the strain regulation effect on the HJFET is more obvious, and the saturation channel current change rate can reach a maximum of about 38%.

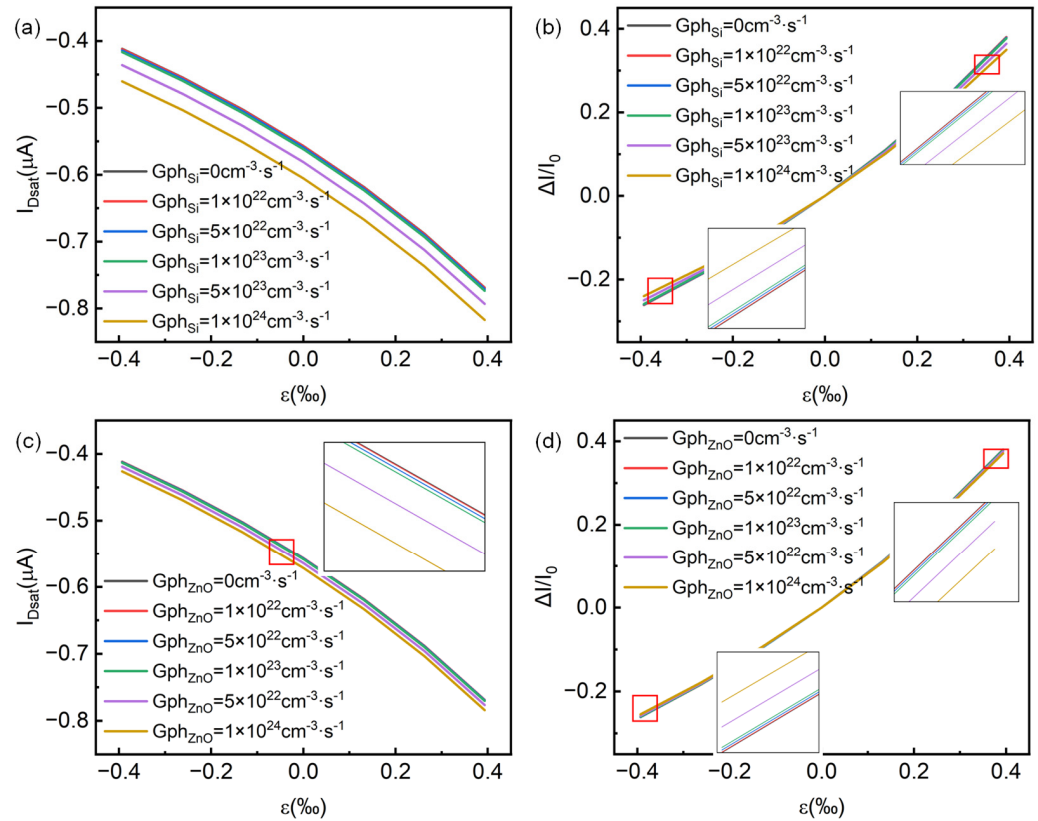


Figure 5. Effect of simultaneously applying strain and light on p-channel HJFET. (a,b) are the saturation current I_{Dsat} and its rate of change $\Delta I/I_0$ with strain ε_3 when only the p-Si channel layer has photo-generated charge carriers. (c,d) are the saturation current I_{Dsat} and its rate of change $\Delta I/I_0$ with strain ε_3 when only the gate n-ZnO layer has photo-generated carriers.

3.2. Effects of Structure Parameters, Doping Concentrations, and Gate Voltages on p-Channel Core-Shell Structure-Based HJFET

In this section, we conducted a scanning analysis of the structural parameters in the p-channel HJFET simulation model, and the results are shown in Figure 6. Figure 6a–c show the scanning results of p-Si channel radius a , and Figure 6d–f show the scanning results of channel length L . From the simulation results, it can be seen that the structural parameter radius a has a greater regulatory effect on device performance. When the radius a varies in the range from 0.25 μm to 0.45 μm , the saturation channel current of the device can increase from -1.31 nA to -4.218 μA . More importantly, the larger radius a , the more the saturated channel current increases when the same strain is applied, i.e., the larger ΔI . However, the saturation channel current change rate becomes smaller, as shown in Figure 6c. At $a = 0.25$ μm and $\varepsilon_3 = 0.39\%$, $\Delta I/I_0$ can reach 192%. The impact of channel length L on device performance is different. The larger channel length L , the smaller the channel current. When the same strain is applied, at $L = 1.2$ μm and $\varepsilon_3 = 0.39\%$, $\Delta I/I_0$ can only reach 43%. The scanning simulation of structural parameters has certain guiding significance for the experimental design of ZnO HJFET. It can be seen from the Figure 6 that the channel thickness a has the greatest influence on the channel current. Therefore, the channel thickness, that is, the Si core diameter, can be determined according to the range of the required channel current. The appropriate device length L is then selected to achieve a specific range of strain sensing.

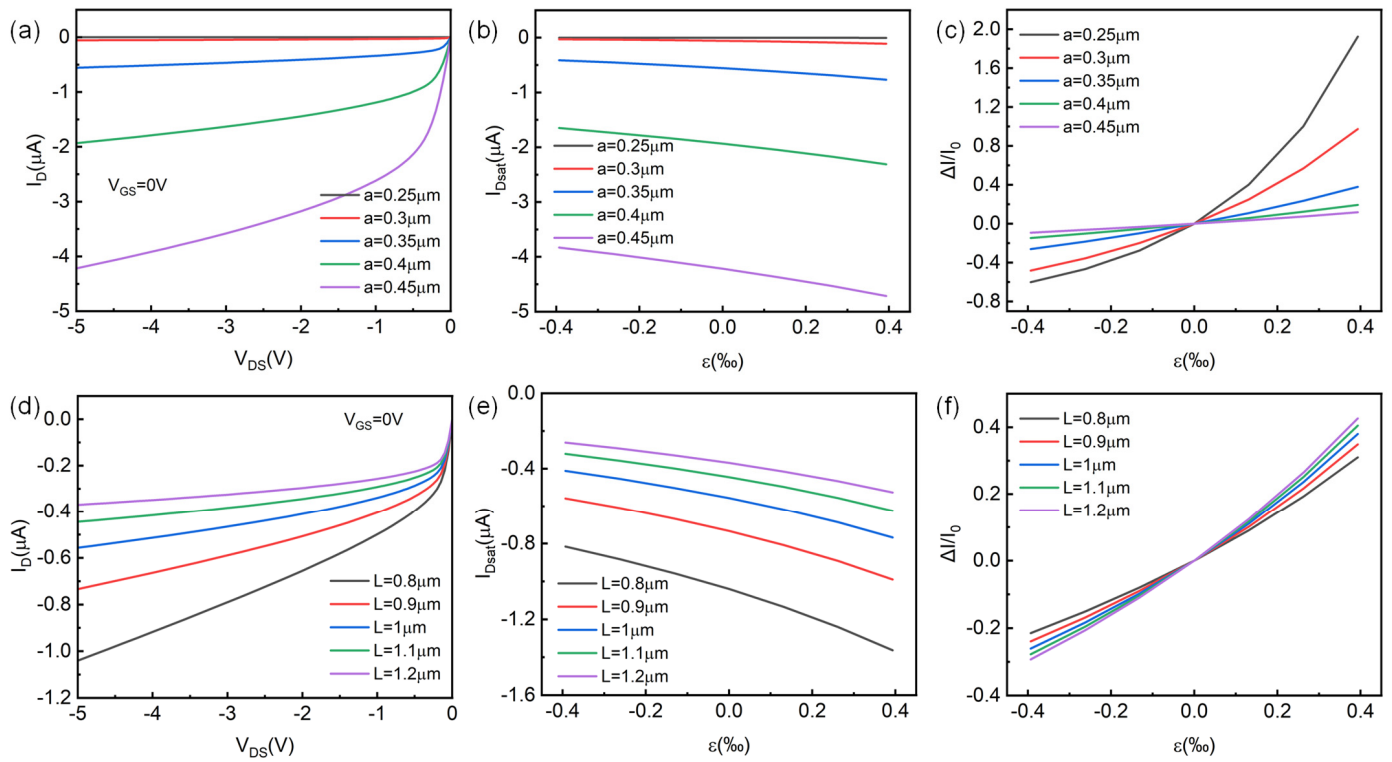


Figure 6. Effect of structural parameters on the piezotronic effect in p-channel HJFET. (a–c) The HJFET output characteristics, saturation current I_{Dsat} , and its rate of change $\Delta I/I_0$ with strain ϵ_3 for different p-Si channel radius a , respectively. (d–f) The HJFET output characteristics, saturation current I_{Dsat} , and its rate of change $\Delta I/I_0$ with strain ϵ_3 for different p-Si channel length L , respectively.

We also conducted a scanning analysis on the doping concentration in the device, and the results are shown in Figure 7. For the convenience of comparative analysis, the parameter values of the scanned donor doping concentration N_D and acceptor doping concentration N_A are the same. From Figure 7a,d, it can be seen that the acceptor doping concentration N_A has a greater impact on the electrical performance of the device. When N_A is at $0.6 \times 10^{16} \text{ cm}^{-3} \sim 1.4 \times 10^{16} \text{ cm}^{-3}$, the saturation channel current of the device can increase from -17 nA to $-2.3 \text{ }\mu\text{A}$. When N_D changes within the same range, the saturated channel current of the device only changes within the range of $-0.494 \text{ }\mu\text{A} \sim -0.668 \text{ }\mu\text{A}$. Furthermore, with the increase in N_A , I_{Dsat} increases and $\Delta I/I_0$ decreases, whereas the impact of N_D on the device is different, with decreasing I_{Dsat} as N_D increases, but decreasing $\Delta I/I_0$. The channel current increases with N_A and decreases with N_D . This is because when N_A increases, the ionized carrier concentration in the channel increases and the channel conductivity increases. At the same time, due to the electrically neutral condition, the width of the depletion layer on the channel side decreases and the channel current increases. However, when N_D increases, the channel conductivity remains unchanged, ignoring the influence of minority carrier electrons, but the width of the channel depletion layer increases, the channel conduction region decreases, and the channel current decreases. Compared with N_A modulation, N_D modulation only changes the width of the channel depletion layer and has less regulatory effect, so the influence of doping concentration in the channel should be mainly considered in the experimental design of ZnO HJFET.

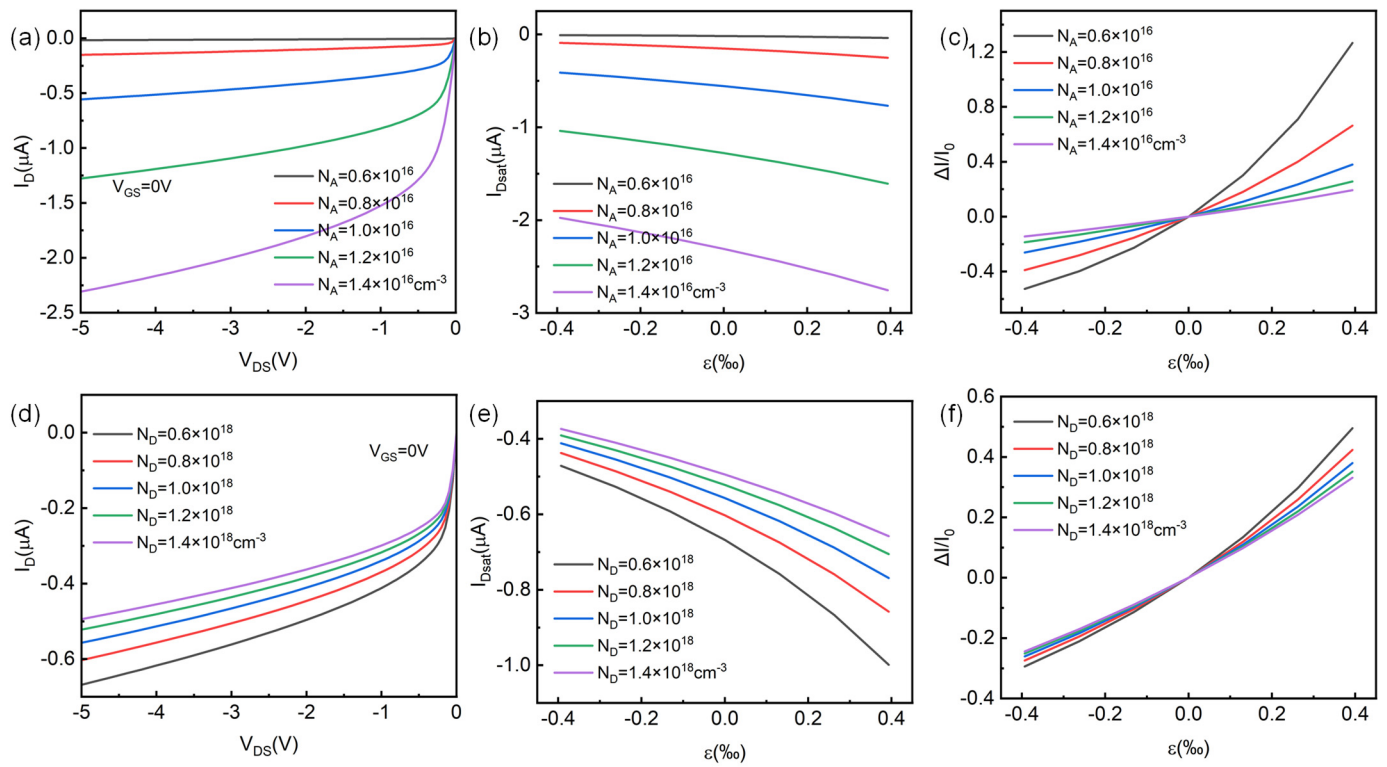


Figure 7. Effect of doping concentration on the piezotronic effect in p-channel HJFET. (a–c) The HJFET output characteristics, saturation current I_{Dsat} , and its rate of change $\Delta I/I_0$ with strain ϵ_3 at different acceptor doping concentrations of N_A , respectively. (d–f) The HJFET output characteristics, saturation current I_{Dsat} , and its rate of change $\Delta I/I_0$ with strain ϵ_3 at different donor doping concentrations of N_D , respectively.

In addition, electric gate voltage can also adjust the channel depletion region width in p-channel HJFET, thus adjusting the channel conductivity and channel current. This working mechanism is similar to the control of structure parameter radius a on device performance, which affects the channel current through changing the thickness of the channel conduction area in the core–shell structure. Consequently, this section mainly studies the piezo-phototronic effect in p-channel HJFET under different gate voltages. Figure 8a–c show the strain regulation effect in HJFET under different gate voltages, and Figure 8d–f show the light regulation effect in HJFET under different gate voltages, with only the case of light absorption in p-Si channel considered. From Figure 8a, it can be seen that after applying tensile strain, the channel current increases and the gate turn-off voltage increases, while applying compressive strain results in the opposite change. From Figure 8b,c, it can be seen that as the forward gate voltage increases, the saturation current of the device decreases, but the rate of saturation current change increases. These results indicate that the influence of gate voltage on the piezotronic effect in the device is consistent with the regulatory effect shown by the aforementioned structural parameter radius a . From Figure 8d–f, it can be seen that the I_D increases with the increase in G_{phSi} . When the forward gate voltage increases, I_D decreases but $\Delta I/I_0$ increases. At $V_{GS} = 0.5$ V and $G_{phSi} = 1 \times 10^{24} \text{ cm}^{-3} \cdot \text{s}^{-1}$, $\Delta I/I_0$ can reach a maximum of about 1924%.

3.3. Piezotronic and Piezo-Phototronic Effects on n-Channel Core–Shell Structure-Based HJFET

Finally, the finite element method-based simulation modeling is carried out for a core–shell structure-based ZnO/Si n-channel nanowire HJFET. The model structure is shown in the inset of Figure 9a. The inner core nanowire is a n-ZnO channel, whose c -axis direction is pointing away from the radial direction, and the outer shell p-Si acts as the gate. If no special instructions are given, this n-channel HJFET is consistent with the model parameters

of the aforementioned p-channel HJFET. In order to ensure that the depletion region is located more in the n-ZnO channel area, the donor concentration N_D in ZnO is adjusted to $1 \times 10^{16} \text{ cm}^{-3}$, and the acceptor concentration N_A in Si is $1 \times 10^{18} \text{ cm}^{-3}$. Figure 9a,b show the transfer characteristics and output characteristics, respectively. Compared with the previously studied p-channel HJFET in Figure 1, the gate turn-off voltage of the n-channel HJFET is slightly higher. When $V_{GS} = -0.25 \text{ V}$ and $V_{DS} = 5 \text{ V}$, the device channel current is about 29.6 nA, while the p-channel HJFET only has a channel current of 2.38 nA under the same bias voltage conditions.

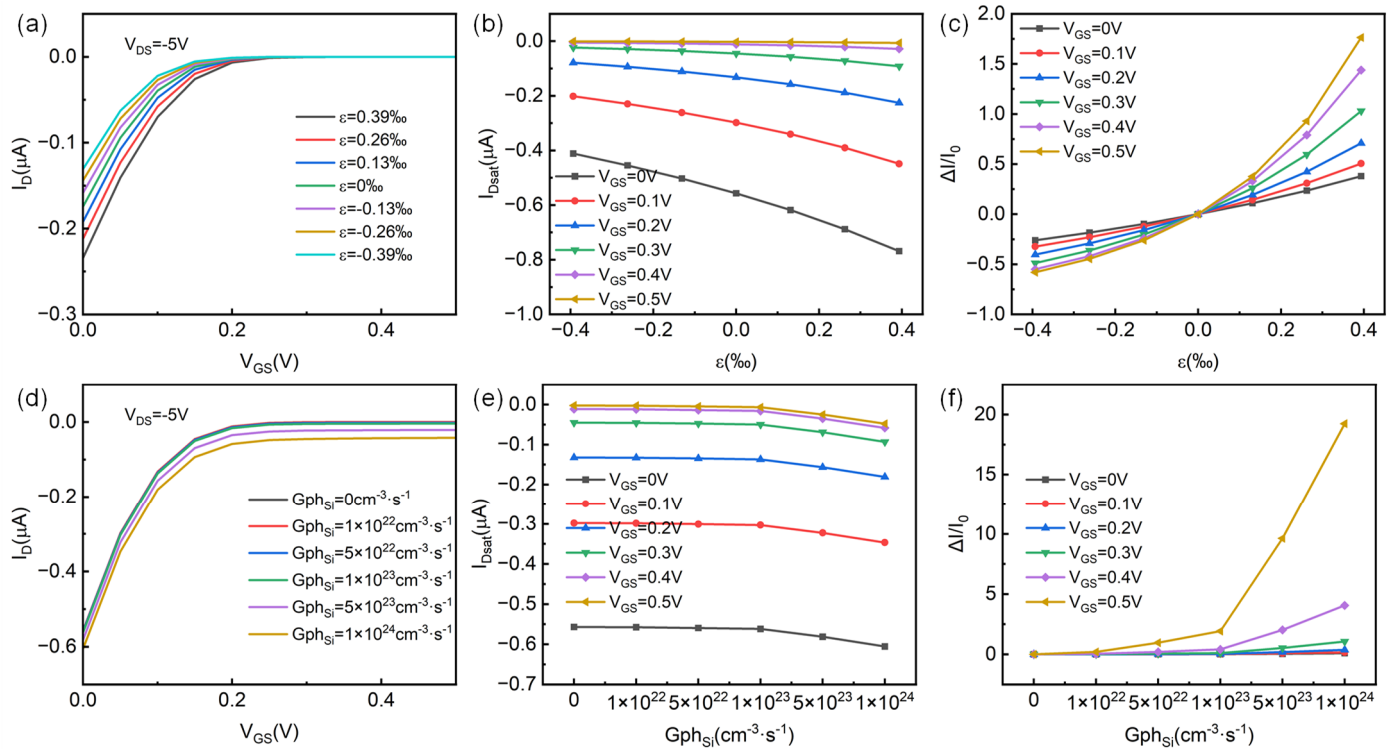


Figure 8. Piezo-phototronic effect in p-channel HJFET under different gate voltage regulation. (a) The transfer characteristics of HJFET under different strain conditions. (b,c) are the saturation current I_{Dsat} and its rate of change $\Delta I/I_0$ with strain ϵ_3 under different gate voltage regulation, respectively. (d) The transfer characteristics of HJFET under different lighting conditions. (e,f) are the saturation current I_{Dsat} and its rate of change $\Delta I/I_0$ with photo-generated carrier generation rate G_{phSi} under different gate voltage regulation, respectively.

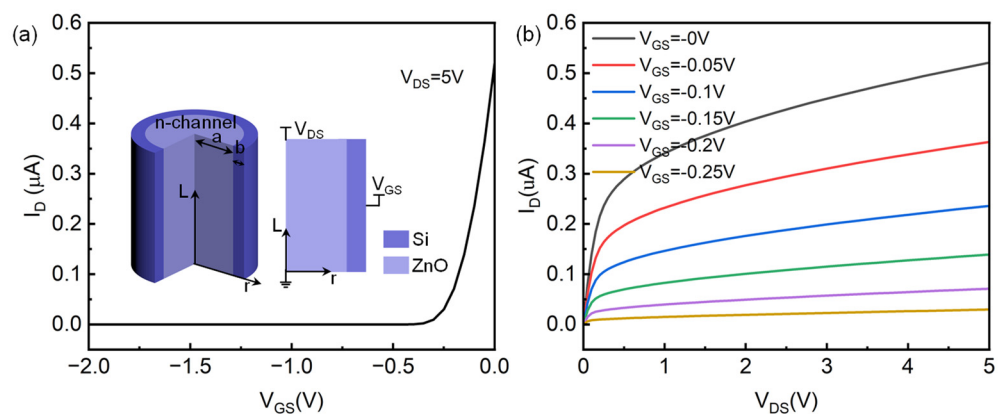


Figure 9. Simulation model and basic characteristics of n-channel HJFET. (a) The transfer characteristics of n-channel HJFET. The inset shows the simulation model and its cross-sectional view. (b) The output characteristics of n-channel HJFET.

The piezo-phototronic effect in the n-channel HJFET based on the core-shell nanowire structure has been simulated and analyzed. Figure 10 shows the changes in channel current under different strains and light illuminations. From the simulation results, it can be seen that the photo-generated carriers in n-ZnO channel have a greater regulatory effect on the device performance. When $G_{ph_{ZnO}} = 1 \times 10^{24} \text{ cm}^{-3} \cdot \text{s}^{-1}$, the saturated channel current is $0.582 \mu\text{A}$, and the generated photocurrent is approximately $0.071 \mu\text{A}$. When the tensile strain is applied, the channel current decreases. When the compressive strain is applied, the channel current increases, which is opposite to the strain regulation in p-channel HJFET. Taking the tensile strain as an example, the negative piezoelectric polarization charges are induced at the interface of the ZnO/Si heterojunction in the n-channel HJFET, resulting in that the channel depletion area increases and hence the channel current decreases. Moreover, the saturation channel current change rate of n-channel HJFET is much smaller. When the externally applied compressive strain ε_3 is -0.39% , the current change rate is only approximately 18%. These results indicate that, for the strain and light cooperated regulation, it might be better to produce the photo-excited charge carriers and the piezoelectric charges at different semiconductors. For instance, the photo-generated carriers are produced in p-Si core channel and the piezoelectric charges are produced in n-ZnO shell gate in the core-shell structure-based Si/ZnO p-channel nanowire HJFET.

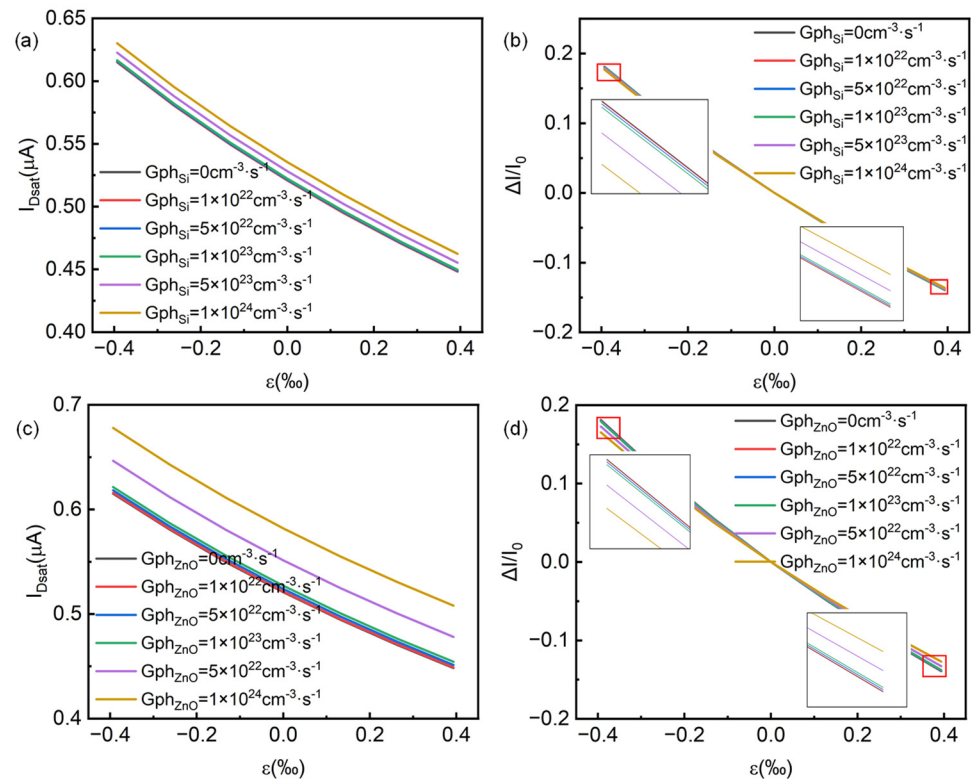


Figure 10. Effect of simultaneously applying strain and light on n-channel HJFET. (a,b) are the saturation current I_{Dsat} and its rate of change $\Delta I/I_0$ with strain ε_3 when only p-Si gate layer has photo-generated charge carriers. (c,d) are the saturation current I_{Dsat} and its rate of change $\Delta I/I_0$ with strain ε_3 when only the n-ZnO channel layer has photo-generated charge carriers.

4. Conclusions

This study mainly uses the finite element method to simulate the core-shell structure-based nanowire HJFET and studies the working mechanisms of piezotronic and piezo-phototronic effects in it. Strain is introduced through the surface charge boundary condition, and light is introduced through a user-defined generation boundary condition. Taking p-channel HJFET as an example, after applying tensile strain, the channel current increases and the saturation current change rate increases. At a tensile strain of 0.39% , the saturation

current change rate can reach 38%. The regulatory mechanism of strain on the electrical performance of HJFET has been analyzed in detail. After applying light, the channel current increases and the saturation current change rate increases. Compared with the photo-generated carriers in the n-ZnO gate, the photo-generated carriers in p-Si channel have a stronger regulatory effect on the device's performance. However, compared to strain regulation, the effect of light regulation is much weaker. Scanning analysis has also been conducted on different parameters, including channel radius a , channel length L , doping concentrations N_A and N_D , and gate voltage V_{GS} . It is concluded that the channel current increases with an increase in radius a and N_A and decreases with an increase in channel length L , N_D , and V_{GS} . The saturation current change rate decreases with the increase in radius a , N_A , and N_D and increases with the increase in channel length L and V_{GS} . Finally, another n-channel HJFET model has been established and simulated to analyze its piezo-phototronic effect. It is found that under the same model parameters, the strain regulation on the saturation current change rate of an n-channel HJFET would be smaller than that of a p-channel HJFET. On the other hand, the light regulation on saturation current change rate of n-channel HJFET would be larger than that of a p-channel HJFET. This work presents that, based on the finite element method, the introduction of strain and light illumination in the simulation model is simple and facile. More importantly, the simulated parameter range of piezoelectric charge density (i.e., the strain) and the location of generation rate (i.e., the light) could be modulated conveniently, not being limited by the necessary assumptions adopted in the analytical derivations. Moreover, the carrier distribution in the whole device could be illustrated to explore the underlying device physics more clearly, providing a more precise understanding of the piezotronic and piezo-phototronic effects in FETs.

Author Contributions: Conceptualization, F.L., W.P. and Y.H.; Methodology, X.L. and F.L.; Software, X.L. and W.P.; Formal analysis, X.L. and W.P.; Investigation, X.L.; Resources, Q.Z., Y.L., G.Z. and H.T.; Data curation, X.L.; Writing—original draft, X.L., F.L. and W.P.; Writing—review & editing, Q.Z., Y.L., G.Z., H.T. and Y.H.; Supervision, W.P. and Y.H.; Funding acquisition, Q.Z., Y.L., G.Z. and H.T. All authors have read and agreed to the published version of the manuscript.

Funding: This research was supported by the National Natural Science Foundation of China (Grant No. 62174131 and 61704135), the China Postdoctoral Science Foundation (Grant No. 2018T111055 and 2017M613138), and the Postdoctoral Research Project of Shaanxi Province (Grant No. 2017BSHEDZZ30).

Data Availability Statement: The research data is available from the corresponding author upon reasonable request.

Conflicts of Interest: The authors declare no conflict of interest.

References

1. Boruah, B.D. Zinc oxide ultraviolet photodetectors: Rapid progress from conventional to self-powered photodetectors. *Nanoscale Adv.* **2019**, *1*, 2059–2085. [[CrossRef](#)]
2. Li, Z.; Li, Z.; Zuo, C.; Fang, X. Application of Nanostructured TiO₂ in UV Photodetectors: A Review. *Adv. Mater.* **2022**, *34*, 2109083. [[CrossRef](#)] [[PubMed](#)]
3. Qu, L.; Ji, J.; Liu, X.; Shao, Z.; Cui, M.; Zhang, Y.; Fu, Z.; Huang, Y.; Yang, G.; Feng, W. Oxygen-vacancy-dependent high-performance α -Ga₂O₃ nanorods photoelectrochemical deep UV photodetectors. *Nano-Technology* **2023**, *34*, 225203. [[CrossRef](#)] [[PubMed](#)]
4. Zhang, M.; Kang, S.; Wang, L.; Zhang, K.; Wu, Y.; Feng, S.; Lu, W. Facile synthesis of β -Ga₂O₃ nanowires network for solar-blind ultraviolet photodetector. *J. Phys. D Appl. Phys.* **2021**, *54*, 175106. [[CrossRef](#)]
5. Gao, J.; Hao, Z.; Niu, L.; Wang, L.; Sun, C.; Xiong, B.; Han, Y.; Wang, J.; Li, H.; Luo, Y.; et al. Surface acoustic wave devices fabricated on epitaxial AlN film. *Funct. Mater. Lett.* **2016**, *9*, 1650034. [[CrossRef](#)]
6. Jaafar, M.M.; Wee, M.F.M.R.; Nguyen, H.-T.; Hieu, L.T.; Rai, R.; Sahoo, A.K.; Dee, C.F.; Chang, E.Y.; Majlis, B.Y.; Tee, C.A.T. Surface Acoustic Wave Propagation of GaN/Sapphire Integrated with a Gold Guiding Layer. *Sensors* **2023**, *23*, 2464. [[CrossRef](#)]
7. Chen, W.; Zhu, Y.; Xiu, J.; Chen, G.; Liang, H.; Liu, S.; Xue, H.; Birgersson, E.; Ho, J.W.; Qin, X.; et al. Monolithic perovskite/organic tandem solar cells with 23.6% efficiency enabled by reduced voltage losses and optimized interconnecting layer. *Nat. Energy* **2022**, *7*, 229–237. [[CrossRef](#)]
8. Witte, W.; Hempel, W.; Paetel, S.; Menner, R.; Hariskos, D. Influence of sputtered gallium oxide as buffer or high-resistive layer on performance of Cu(In,Ga)Se₂-based solar cells. *J. Mater. Res.* **2022**, *37*, 1825–1834. [[CrossRef](#)]

9. Zheng, J.; Wang, G.; Duan, W.; Mahmud, A.; Yi, H.; Xu, C.; Lambertz, A.; Bremner, S.; Ding, K.; Huang, S.; et al. Monolithic Perovskite–Perovskite–Silicon Triple-Junction Tandem Solar Cell with an Efficiency of over 20%. *ACS Energy Lett.* **2022**, *7*, 3003–3005. [[CrossRef](#)]
10. Wang, Z.L. Nanopiezotronics. *Adv. Mater.* **2007**, *19*, 889–892. [[CrossRef](#)]
11. Hu, Y.; Chang, Y.; Fei, P.; Snyder, R.L.; Wang, Z.L. Designing the Electric Transport Characteristics of ZnO Micro/Nanowire Devices by Coupling Piezoelectric and Photoexcitation Effects. *ACS Nano* **2010**, *4*, 1234–1240. [[CrossRef](#)] [[PubMed](#)]
12. An, C.; Qi, H.; Wang, L.; Fu, X.; Wang, A.; Wang, Z.L.; Liu, J. Piezotronic and piezo-phototronic effects of atomically-thin ZnO nanosheets. *Nano Energy* **2021**, *82*, 105653. [[CrossRef](#)]
13. Pan, C.; Zhai, J.; Wang, Z.L. Piezotronics and Piezo-Phototronics of Third Generation Semiconductor Nanowires. *Chem. Rev.* **2019**, *119*, 9303–9359. [[CrossRef](#)] [[PubMed](#)]
14. Wang, Z.L. Piezopotential gated nanowire devices: Piezotronics and piezo-phototronics. *Nano Today* **2010**, *5*, 540–552. [[CrossRef](#)]
15. Wang, Z.L. Progress in Piezotronics and Piezo-Phototronics. *Adv. Mater.* **2012**, *24*, 4632–4646. [[CrossRef](#)]
16. Dai, B.; Biesold, G.M.; Zhang, M.; Zou, H.; Ding, Y.; Wang, Z.L.; Lin, Z. Piezo-phototronic effect on photocatalysis, solar cells, photodetectors and light-emitting diodes. *Chem. Soc. Rev.* **2021**, *50*, 13646–13691. [[CrossRef](#)]
17. Du, X.; Tian, W.; Pan, J.; Hui, B.; Sun, J.; Zhang, K.; Xia, Y. Piezo-phototronic effect promoted carrier separation in coaxial p-n junctions for self-powered photodetector. *Nano Energy* **2022**, *92*, 106694. [[CrossRef](#)]
18. Ouyang, W.; Chen, J.; Shi, Z.; Fang, X. Self-powered UV photodetectors based on ZnO nanomaterials. *Appl. Phys. Rev.* **2021**, *8*, 31315. [[CrossRef](#)]
19. Pan, L.; Sun, S.; Chen, Y.; Wang, P.; Wang, J.; Zhang, X.; Zou, J.; Wang, Z.L. Advances in Piezo-Phototronic Effect Enhanced Photocatalysis and Photoelectrocatalysis. *Adv. Energy Mater.* **2020**, *10*, 2000214. [[CrossRef](#)]
20. Wang, Y.; Xie, W.; Peng, W.; Li, F.; He, Y. Fundamentals and Applications of ZnO-Nanowire-Based Piezotronics and Piezo-Phototronics. *Micromachines* **2023**, *14*, 47. [[CrossRef](#)]
21. Peng, Y.; Lu, J.; Wang, X.; Ma, W.; Que, M.; Chen, Q.; Li, F.; Liu, X.; Gao, W.; Pan, C. Self-powered high-performance flexible GaN/ZnO heterostructure UV photodetectors with piezo-phototronic effect enhanced photoresponse. *Nano Energy* **2022**, *94*, 106945. [[CrossRef](#)]
22. Cho, J.; Hwang, S.; Ko, D.-H.; Chung, S. Transparent ZnO Thin-Film Deposition by Spray Pyrolysis for High-Performance Metal-Oxide Field-Effect Transistors. *Materials* **2019**, *12*, 3423. [[CrossRef](#)] [[PubMed](#)]
23. Ditshego, N.M. ZnO Nanowire Field Effect Transistor for Biosensing: A Review. *J. Nano Res.* **2019**, *60*, 94–112. [[CrossRef](#)]
24. Hwang, J.D.; Chu, C.M. Post oxidation in improving the Schottky-gate MgZnO/ZnO heterojunction field-effect transistors fabricated by RF sputtering. *Mater. Sci. Eng. B* **2021**, *266*, 115063. [[CrossRef](#)]
25. Kato, K.; Matsui, H.; Tabata, H.; Takenaka, M.; Takagi, S. ZnO/Si and ZnO/Ge bilayer tunneling field effect transistors: Experimental characterization of electrical properties. *J. Appl. Phys.* **2019**, *125*, 195701. [[CrossRef](#)]
26. Kim, Y.; Chang, M.; Cho, S.; Kim, M.; Kim, H.; Choi, E.; Ko, H.; Hwang, J.; Park, B. Formation of a functional homo-junction interface through ZnO atomic layer passivation: Enhancement of carrier mobility and threshold voltage in a ZnO nanocrystal field effect transistor. *J. Alloys Compd.* **2019**, *804*, 213–219. [[CrossRef](#)]
27. Seul, H.J.; Kim, M.J.; Yang, H.J.; Cho, M.H.; Cho, M.H.; Song, W.-B.; Jeong, J.K. Atomic Layer Deposition Process-Enabled Carrier Mobility Boosting in Field-Effect Transistors through a Nanoscale ZnO/IGO Heterojunction. *ACS Appl. Mater. Interfaces* **2020**, *12*, 33887–33898. [[CrossRef](#)]
28. Schein, F.-L.; von Wenckstern, H.; Frenzel, H.; Grundmann, M. ZnO-Based n-Channel Junction Field-Effect Transistor with Room-Temperature-Fabricated Amorphous p-Type ZnCo₂O₄ Gate. *IEEE Electron Device Lett.* **2012**, *33*, 676–678. [[CrossRef](#)]
29. Guo, N.; Xiao, L.; Gong, F.; Luo, M.; Wang, F.; Jia, Y.; Chang, H.; Liu, J.; Li, Q.; Wu, Y.; et al. Light-Driven WSe₂-ZnO Junction Field-Effect Transistors for High-Performance Photodetection. *Adv. Sci.* **2020**, *7*, 1901637. [[CrossRef](#)]
30. Ionescu, A.M.; Riel, H. Tunnel field-effect transistors as energy-efficient electronic switches. *Nature* **2011**, *479*, 329–337. [[CrossRef](#)]
31. Afzal, A.; Doornbos, G.; Shen, T.-M.; Passlack, M.; Wu, J. A High-Performance InAs/GaSb Core-Shell Nanowire Line-Tunneling TFET: An Atomistic Mode-Space NEGF Study. *IEEE J. Electron Devices Soc.* **2019**, *7*, 88–99. [[CrossRef](#)]
32. Kumar, N.; Mushtaq, U.; Amin, S.I.; Anand, S. Design and performance analysis of Dual-Gate All around Core-Shell Nanotube TFET. *Superlattices Microstruct.* **2019**, *125*, 356–364. [[CrossRef](#)]
33. Kumar Singh, N.; Kar, R.; Mandal, D. Design of Si_{0.45}Ge_{0.55}-based core-shell-type dual-material dual-gate nanotube TFET with source pocket technique. *Appl. Phys. A* **2021**, *127*, 233. [[CrossRef](#)]
34. Li, F.; Peng, W.; He, Y. Bilateral piezoelectric charge modulation as a perspective of piezo-phototronic effect in tri-/multi-layer structured optoelectronics. *Nano Energy* **2023**, *113*, 108537. [[CrossRef](#)]
35. Peng, W.; Wang, C.; Li, F.; He, Y. Piezo- and photo-voltage field-effect transistor. *Nano Energy* **2023**, *105*, 108025. [[CrossRef](#)]

Disclaimer/Publisher’s Note: The statements, opinions and data contained in all publications are solely those of the individual author(s) and contributor(s) and not of MDPI and/or the editor(s). MDPI and/or the editor(s) disclaim responsibility for any injury to people or property resulting from any ideas, methods, instructions or products referred to in the content.